

EXPERIMENTAL DETERMINATION OF PHASE EQUILIBRIA AT 900 °C AND LIQUIDUS SURFACE IN THE Cu-Ni-Ti SYSTEM

B. Jin ^a, X. Lu ^b, S. Liu ^{a*}, D. Huang ^c, Y. Du ^a^a Central South University, State Key Laboratory of Powder Metallurgy, Changsha, China^b University of Connecticut, Department of Materials Science and Engineering & Institute of Materials Science, Storrs, USA^c Guangxi University, Guangxi Key Laboratory of Processing for Non-ferrous Metal and Featured Materials, Nanning, China

(Received 9 February 2018; accepted 29 March 2018)

Abstract

Phase equilibria at 900 °C and the liquidus projection in the Ni-rich corner of the Cu-Ni-Ti ternary system were investigated by X-ray diffraction (XRD), scanning electron microscopy (SEM), electron probe microanalysis (EPMA) and differential scanning calorimetry (DSC) on the annealed and as-cast alloys. For the isothermal section at 900 °C, the high-temperature ternary compound (τ_3) reported in the literature was not observed but the corresponding low-temperature compound (τ_6) was identified to be stable at this temperature. For the liquidus projection, the primary phase τ_4 was experimentally determined for the first time, and the related solidification paths were identified through the experimental data on the as-cast alloys. One solid-state invariant reaction, $\text{NiTi} + \tau_4 \rightarrow \tau_1 + \text{Ni}_3\text{Ti}$ at 1098.3 °C and two ternary eutectic reactions, $L \rightarrow \tau_1 + \tau_4 + \text{NiTi}$ at 1126 °C and $L \rightarrow \tau_1 + \tau_6 + \text{fcc}(\text{Cu,Ni})$ at 1069.5 °C were detected. Scheil reaction scheme was also presented accordingly. All obtained experimental results will provide reliable information for further thermodynamic optimization of the Cu-Ni-Ti ternary system.

Keywords: Cu-Ni-Ti; Isothermal section; Thermal analysis; Liquidus projection; Reaction scheme**1. Introduction**

Shape memory alloys (SMAs) have been extensively investigated as an important category of functional materials for their potential applications in different engineering areas, such as composite materials, automotive, aerospace, mini actuators and micro-electromechanical systems (MEMS), robotics, as well as certain biomedical applications [1]. Among various SMA systems, near-equiatomic NiTi alloys attract the highest technological interest because of their abilities to change shapes with temperature or load to provide controllable material and damping properties [2, 3]. The addition of Cu into the NiTi alloys can substitute for the Ni-sites in B2 phase (NiTi), which can considerably narrow the transformation temperature hysteresis [4, 5], reduce the sensitivity of M_s to the Ni:Ti ratio [6], increase the strength difference between the parent and martensite phases and improve the transformational cyclic behavior [7]. It was also reported that the amount of Cu substitution for Ni affects the transformation sequence [4]. Moreover, the Cu-Ni-Ti alloys are good potential damping materials [8] and exhibit prominent glass forming ability through both rapid solidification

processing and mechanical alloying [9]. Therefore, in order to achieve the rational design of high-performance Cu-Ni-Ti shape memory alloys, the knowledge of phase equilibria and solidification sequence of the Cu-Ni-Ti system is of great necessity.

The phase diagrams of the three sub-binary systems have been well established, as shown in Fig. 1. The Cu-Ti and Ni-Ti phase diagrams are characterized with multiple binary compounds, whereas Cu-Ni is an isomorphous phase diagram with spinodal decomposition of the fcc(Cu,Ni) phase at low temperature [10, 11].

According to review work by Schuster and Cacciamani [12], there are six ternary compounds stable in the Cu-Ni-Ti ternary system, which are summarized in Table 1. Several groups have contributed to the isothermal sections of the Cu-Ni-Ti system. The isothermal section of Cu-Ni-Ti at 800 °C over the whole composition range was investigated by Pfeifer et al. [13] using XRD, but the annealing time was too short (i.e. 2 h) in their work. Subsequently, Fedorov et al. [14] constructed the partial isothermal sections at 850 and 1000 °C in the Cu-rich corner by XRD method. It is worth mentioning that Fedorov et al. [14] have not observed τ_4 and τ_6 in their samples,

*Corresponding author: shliu@csu.edu.cn



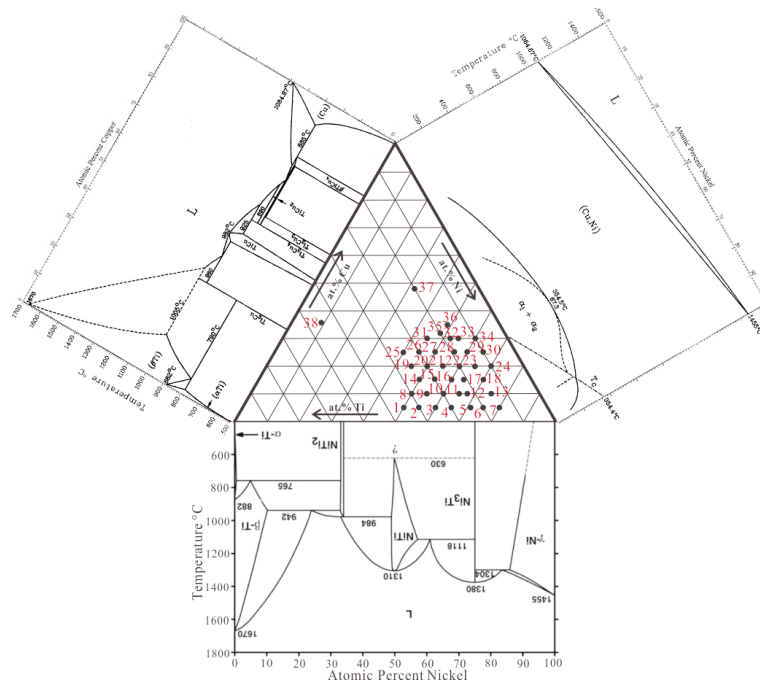


Figure 1. Binary phase diagrams [10, 11] of the Cu-Ni-Ti system along with the composition points of the alloys studied in the present work

Cu-Ni₃Ti [21, 22], NiTi-CuNiTi [23], Cu-CuNiTi [16], CuTi-CuNiTi [23], and CuTi-NiTi [23-25] sections have been presented by several groups. These sections were initially presented as pseudobinary systems. Later, the work by Zhang et al. [17] and Zhu et al. [18] showed that the CuTi-NiTi section was not a pseudobinary phase diagram. The phase equilibria presented for these sections are probably reliable in the temperature range where the liquid phase is involved in the equilibria [12].

The experimental data on liquidus projection and invariant reactions are mostly available for the Cu-rich and Ti-rich regions. In the Ti-CuTi-NiTi region, one reaction of transition type, Liquid + NiTi \leftrightarrow CuTi + NiTi₂, and two ternary eutectic reactions, Liquid \leftrightarrow CuTi + CuTi₂ + NiTi₂ and Liquid \leftrightarrow bcc(Ti) + CuTi₂ + NiTi₂ were proposed by Gupta [39]. However, these reactions are in contradiction to the review of Schuster and Cacciamani [12], in which CuTi cannot coexist with NiTi₂ on the liquidus surface. In the work by Schuster and Cacciamani [12], two U-type reactions, Liquid + bcc(Ti) \leftrightarrow CuTi₂ + NiTi₂ and Liquid + CuTi \leftrightarrow CuTi₂ + NiTi, and one ternary eutectic reaction as Liquid \leftrightarrow NiTi + CuTi₂ + NiTi₂, were reported. This liquidus projection is also questionable because the range of the primary CuTi₂ phase is in contradiction to the liquidus in the Cu-Ti binary system [11]. Furthermore, a ternary eutectoid reaction as bcc(Ti) \leftrightarrow CuTi₂ + NiTi₂ + hep(Ti) at 738 °C was proposed by Yakushiji et al. [19] and accepted by other researchers [12].

In the CuTi-NiTi-Cu region, a series of invariant

reactions were reported by Fedorov et al. [14], Yakushiji et al. [40], and Alisova et al. [41]. These reactions were accepted in the critical review of Schuster and Cacciamani [12]. However, a few modifications are required for some invariant reactions to achieve the consistency with the isothermal section at 870 °C, proposed by Loo et al. [15]. For example, according to the reaction scheme [12] the three-phase CuTi + NiTi + τ_1 field should exist down to the room temperature, which is in contradiction to the experimental data [15, 17, 18].

For the Cu-Ni-NiTi region, the experimental information of the phase equilibria and invariant reactions is far from being established. Considering this situation, further investigations are needed to determine the phase relations and liquidus projection in this region.

The objective of the present work is to clarify the conflicts on the phase equilibria in literature and provide more accurate experimental data for further thermodynamic optimization of the Cu-Ni-Ti ternary system. With this purpose, we chose the isothermal section at 900 °C to investigate, and we tried to obtain the whole liquidus projection of the Cu-Ni-Ti system using both the annealed and as-cast alloys.

2. Experimental procedure

Thirty-eight ternary alloys were prepared from Ni, Ti and Cu rods (Beijing KMT Technology Co. Ltd., China) of 99.99 wt.% purity in an arc melting furnace (WKDHL-I, Opto-electronics Co. Ltd., Beijing,

Table 1. Crystal structures and lattice parameters of the phases in the Cu-Ni-Ti system

Phase	Pearson symbol	Space group	Prototype	Lattice parameter (nm)	Ref.
(Ni)	<i>cF4</i>	<i>Fm-3m</i> (225)	Cu	<i>a</i> =0.3586	[26]
(βTi)	<i>cI2</i>	<i>Im-3m</i> (229)	W	<i>a</i> =0.333	[27]
(αTi)	<i>hP2</i>	<i>P6₃/mmc</i> (194)	Mg	<i>a</i> =0.29486 <i>c</i> =0.467	[28]
(Cu)	<i>cF4</i>	<i>Fm-3m</i> (225)	Cu	<i>a</i> =0.3615	[29]
Ni ₃ Ti	<i>hP16</i>	<i>P6₃/mmc</i> (194)	Ni ₃ Ti	<i>a</i> =0.5109 <i>c</i> =0.8299	[30]
NiTi	<i>cP2</i>	<i>Pm-3m</i> (221)	CsCl	<i>a</i> =0.3015	[31]
NiTi ₂	<i>cF96</i>	<i>Fd-3m</i> (227)	NiTi ₂	<i>a</i> =1.13193	[32]
Cu ₄ Ti	<i>oP20</i>	<i>Pnma</i> (62)	Au ₄ Zr	<i>a</i> =0.4526 <i>b</i> =0.4345 <i>c</i> =1.2924	[33]
Cu ₂ Ti	<i>oS12</i>	<i>Cmcm</i> (63)	Au ₂ V	<i>a</i> =0.7988 <i>b</i> =0.4458 <i>c</i> =0.4397	[34]
Cu ₃ Ti ₂	<i>tP10</i>	<i>P4/nmm</i> (129)	Cu ₃ Ti ₂	<i>a</i> =0.313 <i>c</i> =1.395	[35]
Cu ₄ Ti ₃	<i>tI14</i>	<i>I4/mmm</i> (139)	Cu ₄ Ti ₃	<i>a</i> =0.3126 <i>c</i> =1.9964	[36]
CuTi	<i>tP4</i>	<i>P4/nmm</i> (129)	CuTi	<i>a</i> =0.3107 <i>c</i> =0.5919	[36]
CuTi ₂	<i>tI6</i>	<i>I4/mmm</i> (139)	CuZr ₂	<i>a</i> =0.29438 <i>c</i> =1.07861	[32]
τ ₁ TiNiCu	<i>tI6</i>	<i>I4/mmm</i> (139)	MoSi ₂	<i>a</i> =0.312 <i>c</i> =0.7965	[15]
τ ₂ Ti ₂ (NiCu) ₃	<i>tP10</i>	<i>P4/nmm</i> (129)	Cu ₃ Ti ₂	<i>a</i> =0.44028 <i>c</i> =1.3525	[15]
τ ₃ Ti ₂ (NiCu) ₃	orthor.	N.A.	N.A.	<i>a</i> =0.4620 <i>b</i> =0.4522 <i>c</i> =1.3194	[37]
τ ₄ Ti ₅ Ni ₄ Cu	<i>hR36</i>	<i>R-3m</i> (166)	BaPb ₃	<i>a</i> =0.5112 <i>b</i> =0.5112 <i>c</i> =1.8871 <i>α</i> =90 ° <i>β</i> =90 ° <i>γ</i> =120 °	[38]
τ ₅ TiNi ₂ Cu	<i>oP8</i>	<i>Pmmn</i>	Cu ₃ Sb	<i>a</i> =0.5067 <i>b</i> =0.4216 <i>c</i> =0.4495	[38]
τ ₆ TiNi ₂ Cu	<i>tI8</i>	<i>I4/mmm</i> (139)	TiAl ₃	<i>a</i> =0.3611 <i>c</i> =0.7459	[15]
τ ₇ Ti ₁₀ Ni ₂₉ Cu	<i>hP40</i>	<i>P6₃/mmc</i> (194)	Pd ₂ RhTa	<i>a</i> =0.5116 <i>c</i> =2.090	[38]



Table 2. Summary of the phases and their compositions in the equilibrated Cu-Ni-Ti alloys after heat treatment at 900 °C for 960 h

Alloy		Equilibrated phases according XRD	Phase composition (at.%)		
NO.	Composition (at.%)		Ni	Ti	Cu
1	Ni50-Ti45-Cu5	τ_1	49.32	33.88	16.8
		NiTi	50.51	46.49	3
3	Ni60-Ti35-Cu5	τ_1	53.92	33.37	12.71
		NiTi	52.39	45.25	2.36
		Ni_3Ti	71.79	25.36	2.85
5	Ni71.25-Ti23.75-Cu5	Ni_3Ti	72.23	24.22	3.55
		fcc(Cu,Ni)	30.6	9.73	59.67
6	Ni75-Ti20-Cu5	Ni_3Ti	74.03	22.8	3.17
		fcc(Cu,Ni)	74.32	12.12	13.56
7	Ni80-Ti15-Cu5	Ni_3Ti	76.51	20.08	3.41
		fcc(Cu,Ni)	82.65	9.1	8.25
9	Ni55-Ti35-Cu10	τ_1	53.4	33.78	12.82
		NiTi	51.62	45.94	2.43
		Ni_3Ti	71.41	25.34	3.25
10	Ni60-Ti30-Cu10	τ_1	50.39	34.23	15.39
		Ni_3Ti	70.34	26.06	3.6
11	Ni65-Ti25-Cu10	τ_4	67.73	24.8	7.47
		τ_6	51.22	24.68	24.11
15	Ni55-Ti30-Cu15	τ_1	44.89	33.92	21.19
		τ_4	67.09	26.03	6.88
16	Ni60-Ti25-Cu15	τ_4	66.42	25.81	7.76
		τ_6	50.87	25.48	23.65
18	Ni70-Ti15-Cu15	Ni_3Ti	73.1	22.86	4.04
		fcc(Cu,Ni)	63.46	6.32	30.22
20	Ni50-Ti30-Cu20	τ_1	43.45	34	22.55
		τ_4	66.79	25.88	7.33
		τ_6	49.47	25.9	24.63
22	Ni60-Ti20-Cu20	Ni_3Ti	72.86	23.21	3.93
		fcc(Cu,Ni)	9.71	0.17	90.12
26	Ni45-Ti30-Cu25	τ_1	43.25	32.94	23.81
		τ_6	47.8	25.63	26.57
28	Ni56.25-Ti18.75-Cu25	Ni_3Ti	69.37	24.61	6.02
		fcc(Cu,Ni)	6.6	0.81	92.59
29	Ni60-Ti15-Cu25	Ni_3Ti	71.93	23.29	4.77
		fcc(Cu,Ni)	34.61	1.78	63.61
32	Ni52.5-Ti17.5-Cu30	fcc(Cu,Ni)	7.33	0.95	91.72
		Ni_3Ti	69.2	23.63	7.17
33	Ni55-Ti15-Cu30	Ni_3Ti	70.38	22.7	6.92
		fcc(Cu,Ni)	22.86	0.95	76.19
35	Ni48-Ti20-Cu32	τ_4	65.94	25.98	8.08
		τ_6	49.13	25.98	24.89
		fcc(Cu,Ni)	3.67	0.98	95.35
37	Ni32-Ti20-Cu48	τ_6	47.69	25.96	26.35
		τ_1	42.22	33.82	23.96
		fcc(Cu,Ni)	3.34	1.28	95.38
38	Ni9-Ti55-Cu36	NiTi	16.35	51.08	32.57
		CuTi	2.69	51.45	45.86
		$CuTi_2$	5.17	66.76	28.07



Table 3. Summary of the primary phases and solidification paths of the Cu-Ni-Ti as-cast alloys

Alloy		Primary phase	Phases according XRD	Solidification path
NO.	Composition (at.%)			
1	Ni50-Ti45-Cu5	NiTi	NiTi	L → NiTi
			τ_1	L → NiTi + τ_1
2	Ni55-Ti40-Cu5	NiTi	NiTi	L → NiTi
			τ_1	L → NiTi + τ_1
8	Ni50-Ti40-Cu10	NiTi	NiTi	L → NiTi
			τ_1	L → NiTi + τ_1
9	Ni55-Ti35-Cu10	τ_1	τ_1	L → τ_1
			NiTi	L → NiTi + τ_1
14	Ni50-Ti35-Cu15	τ_1	τ_1	L → τ_1
			NiTi	L → NiTi + τ_1
19	Ni45-Ti35-Cu20	τ_1	τ_1	L → τ_1
			NiTi	L → NiTi + τ_1
25	Ni40-Ti35-Cu25	τ_1	τ_1	L → τ_1
			NiTi	L → NiTi + τ_1
26	Ni45-Ti30-Cu25	τ_1	τ_1	L → τ_1
			τ_6	L → τ_1 + τ_6
			fcc(Cu,Ni)	L → τ_1 + τ_6 + fcc(Cu,Ni)
3	Ni60-Ti35-Cu5	τ_4	τ_4	L → τ_4
			NiTi	L → τ_4 + NiTi
			τ_1	L → τ_4 + NiTi + τ_1
4	Ni65-Ti30-Cu5	τ_4	τ_4	L → τ_4
			τ_1	L → τ_4 + τ_1
			NiTi	L → τ_4 + τ_1 + NiTi
10	Ni60-Ti30-Cu10	τ_4	τ_4	L → τ_4
			τ_1	L → τ_4 + τ_1
			NiTi	L → τ_4 + τ_1 + NiTi
11	Ni65-Ti25-Cu10	τ_4	τ_4	L → τ_4
			τ_6	L → τ_4 + τ_6
			τ_1	L → τ_4 + τ_6 + τ_1
16	Ni60-Ti25-Cu15	τ_4	τ_4	L → τ_4
			τ_6	L → τ_4 + τ_6
			τ_1	L → τ_4 + τ_6 + τ_1
20	Ni50-Ti30-Cu20	τ_6	τ_6	L → τ_6
			τ_1	L → τ_6 + τ_1
27	Ni50-Ti25-Cu25	τ_6	τ_6	L → τ_6
			τ_1	L → τ_6 + τ_1
			fcc(Cu,Ni)	L → τ_6 + τ_1 + fcc(Cu,Ni)
31	Ni45-Ti25-Cu30	τ_6	τ_6	L → τ_6
			τ_1	L → τ_6 + τ_1
			fcc(Cu,Ni)	L → τ_6 + τ_1 + fcc(Cu,Ni)
35	Ni48-Ti20-Cu32	τ_6	τ_6	L → τ_6
			τ_1	L → τ_6 + τ_1
			fcc(Cu,Ni)	L → τ_6 + τ_1 + fcc(Cu,Ni)
37	Ni32-Ti20-Cu48	τ_6	τ_6	L → τ_6
			τ_1	L → τ_6 + τ_1
			fcc(Cu,Ni)	L → τ_6 + τ_1 + fcc(Cu,Ni)
5	Ni71.25-Ti23.75-Cu5	Ni ₃ Ti	Ni ₃ Ti	L → Ni ₃ Ti
			fcc(Cu,Ni)	L → Ni ₃ Ti + fcc(Cu,Ni)
12	Ni67.5-Ti22.5-Cu10	Ni ₃ Ti	Ni ₃ Ti	L → Ni ₃ Ti
			fcc(Cu,Ni)	L → Ni ₃ Ti + fcc(Cu,Ni)
17	Ni63.75-Ti21.25-Cu15	Ni ₃ Ti	Ni ₃ Ti	L → Ni ₃ Ti
			fcc(Cu,Ni)	L → Ni ₃ Ti + fcc(Cu,Ni)

Table 3 continues on next page



Table 3 continues from the previous page

22	Ni60-Ti20-Cu20	Ni ₃ Ti	Ni ₃ Ti	L → Ni ₃ Ti
			fcc(Cu,Ni)	L → Ni ₃ Ti + fcc(Cu,Ni)
28	Ni56.25-Ti18.75-Cu25	Ni ₃ Ti	Ni ₃ Ti	L → Ni ₃ Ti
			fcc(Cu,Ni)	L → Ni ₃ Ti + fcc(Cu,Ni)
32	Ni52.5-Ti17.5-Cu30	Ni ₃ Ti	Ni ₃ Ti	L → Ni ₃ Ti
			fcc(Cu,Ni)	L → Ni ₃ Ti + fcc(Cu,Ni)
36	Ni48.75-Ti16.25-Cu35	Ni ₃ Ti	Ni ₃ Ti	L → Ni ₃ Ti
			fcc(Cu,Ni)	L → Ni ₃ Ti + fcc(Cu,Ni)
6	Ni75-Ti20-Cu5	Ni ₃ Ti	Ni ₃ Ti	L → Ni ₃ Ti
			fcc(Cu,Ni)	L → Ni ₃ Ti + fcc(Cu,Ni)
29	Ni60-Ti15-Cu25	Ni ₃ Ti	Ni ₃ Ti	L → Ni ₃ Ti
			fcc(Cu,Ni)	L → Ni ₃ Ti + fcc(Cu,Ni)
33	Ni55-Ti15-Cu30	Ni ₃ Ti	Ni ₃ Ti	L → Ni ₃ Ti
			fcc(Cu,Ni)	L → Ni ₃ Ti + fcc(Cu,Ni)
13	Ni75-Ti15-Cu10	Ni ₃ Ti	Ni ₃ Ti	L → Ni ₃ Ti
			fcc(Cu,Ni)	L → Ni ₃ Ti + fcc(Cu,Ni)
18	Ni70-Ti15-Cu15	Ni ₃ Ti	Ni ₃ Ti	L → Ni ₃ Ti
			fcc(Cu,Ni)	L → Ni ₃ Ti + fcc(Cu,Ni)
23	Ni65-Ti15-Cu20	Ni ₃ Ti	Ni ₃ Ti	L → Ni ₃ Ti
			fcc(Cu,Ni)	L → Ni ₃ Ti + fcc(Cu,Ni)
7	Ni80-Ti15-Cu5	fcc(Cu,Ni)	fcc(Cu,Ni)	L → fcc(Cu,Ni)
24	Ni70-Ti10-Cu20	fcc(Cu,Ni)	fcc(Cu,Ni)	L → fcc(Cu,Ni)
30	Ni65-Ti10-Cu25	fcc(Cu,Ni)	fcc(Cu,Ni)	L → fcc(Cu,Ni)
34	Ni60-Ti10-Cu30	fcc(Cu,Ni)	fcc(Cu,Ni)	L → fcc(Cu,Ni)



China) under high purity argon atmosphere using a non-consumable W electrode. The ingots were remelted 4 times to improve their homogeneity. No chemical analysis for the alloys was conducted since the weight loss of each alloy during the arc-melting process was less than 1 wt.%. Afterwards, the ingots were generally cut into two pieces. One was kept as-cast and subjected to the microstructure observation to investigate the primary solidification phase and reaction type. The other was annealed and subjected to XRD, SEM, EPMA and DSC. These alloys were wrapped in Mo wires after mechanical polishing of the surfaces and then sealed in evacuated silica capsules for annealing in an L4514-type diffusion furnace (Qingdao Instrument & Equipment Co. Ltd., China) at 900 °C for 960 hours, followed by quenching in liquid nitrogen. The nominal composition for each alloy are shown in Fig. 1 and Tables 2 and 3.

X-ray diffraction (XRD) measurements were performed on a Rigaku D-max/2250 VB+ X-ray diffractometer at 40 kV and 250 mA using a Cu-K α radiation. Microstructure observations of the alloys in both as-cast or annealed states were conducted using scanning electron microscopy with energy dispersive X-ray analysis (SEM/EDX, Nova NanoSEM-230, USA) after standard metallographic preparation. The primary solidification phases and reaction types were determined from the backscattered electron (BSE) images of the as-cast alloys. The composition analysis of both as-cast and annealed specimens were performed by electron probe microanalysis (EPMA, JXA-8530, JEOL, Japan) at 15 kV with pure Ni (99.99 wt.%), Ti (99.99 wt.%) and Cu (99.99 wt.%) as

standard materials. The phase transition temperatures were measured by differential scanning calorimetry (DSC) (DSC404C, Netzsch, Germany) of the annealed alloys 3#, 9# and 37#. The measurements were performed between 900 °C and 1300 °C with the heating and cooling rates of 5 K/min under a flowing argon atmosphere using the Al₂O₃ crucible. The temperatures of invariant reactions were determined from the onset of the thermal effects on the heating curve, while those for liquidus were taken from the tangential intersection of the last peak of the heating curve. The analyses of relevant cooling curve are also enclosed for comparison, as listed in Table 4.

3. Results and discussion

3.1. Phase equilibria at 900 °C

The selected annealed alloys along with the measured constituent phases and compositions by XRD and EPMA are listed in Table 2. In Fig. 2, the microstructures of the alloys 20#, 26#, 16#, 15#, 37# and 35# annealed at 900 °C for 960 h are shown in the BSE images. Phase equilibria of $\tau_1 + \tau_4 + \tau_6$ in the alloy 20#, $\tau_1 + \tau_6$ in the alloy 26#, $\tau_4 + \tau_6$ in the alloy 16#, $\tau_1 + \tau_4$ in the alloy 15#, fcc(Cu,Ni) + $\tau_1 + \tau_6$ in the alloy 37# and fcc(Cu,Ni) + $\tau_4 + \tau_6$ in the alloy 35# were observed, as shown in Figs. 2(a)-(f), and the respective XRD patterns are presented in Fig. 3. The τ_5 phase, which was deduced considering a weak DSC thermal signal with a heating rate of 40 K/min by Zhu et al. [18] at 900 °C, was not observed in this work, but the τ_6 phase was found instead.

Fig. 4 shows the microstructures of the alloys 1#, 22#, 3#, 10# and 38# annealed at 900 °C for 960 h.

Table 4. Temperatures extracted from the DSC curves in the Cu-Ni-Ti system and their interpretation

Alloy		Temperature (°C)		Interpretation	Remarks
NO.	Composition (at.%)	Heating	Cooling		
3	Ni60-Ti35-Cu5	1098.3 ^s	1095.3 ^s	NiTi + $\tau_4 \rightarrow \text{Ni}_3\text{Ti} + \tau_1$	Invariant reaction
		Not detec.	1102.7 ^s	L $\rightarrow \tau_4 + \text{NiTi} + \tau_1$	Invariant reaction
		1135.4 ^s	Not detec.	L + $\tau_4/\text{L} + \tau_4 + \text{NiTi}$	
		Not detec.	1213.6 ^s	L/L + τ_4	Primary phase formation
9	Ni55-Ti35-Cu10	1098.4 ^s	1092.2 ^s	NiTi + $\tau_4 \rightarrow \text{Ni}_3\text{Ti} + \tau_1$	Invariant reaction
		1126.0 ^w	Not detec.	L $\rightarrow \tau_1 + \text{NiTi} + \tau_4$	Invariant reaction
		1139.2 ^s	1130.7 ^s	L + $\tau_1/\text{L} + \tau_1 + \text{NiTi}$	
		Not detec.	1152.7 ^s	L/L + τ_1	Primary phase formation
37	Ni32-Ti20-Cu48	1069.5 ^s	1065.3 ^s	L $\rightarrow \tau_6 + \tau_1 + (\text{Cu,Ni})$	Invariant reaction
		1090.1 ^s	1081.7 ^s	L + $\tau_6/\text{L} + \tau_6 + \tau_1$	
		1137.2 ^s	1117.4 ^s	L/L + τ_6	Primary phase formation

^s strong and clear signal; ^w weak signal; Not detec. Not detected



According to Fig. 4(a), there are two phases in the annealed alloy #1. According to the XRD results shown in Table 2, the matrix is the NiTi phase and the second phase is τ_1 distributed randomly. In Fig. 4(b) of the annealed alloy 22#, there are two phases - Ni₃Ti wrapped in the net of fcc(Cu,Ni). It was also established that the microstructure of the alloy 3# is τ_1 + NiTi + Ni₃Ti (Fig. 4(c)). τ_1 + Ni₃Ti was observed in

the annealed alloy 10# (Fig. 4(d)), and the NiTi + CuTi + CuTi₂ structures was observed in the annealed alloy 38# (Figs. 4(e)).

Based on the above analysis of BSE images and XRD patterns in this work and the literature data [10, 11, 18, 20], the isothermal section of Cu-Ni-Ti system at 900 °C was constructed in Fig. 5. Comparing to the

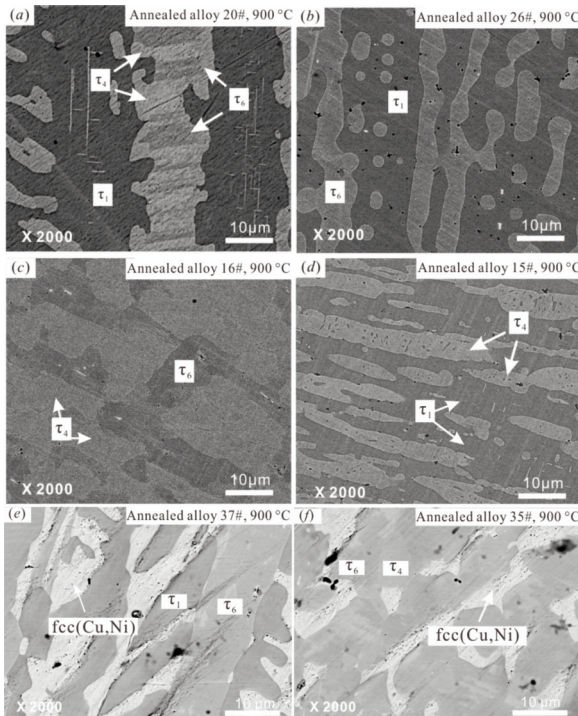


Figure 2. BSE images of the annealed Cu-Ni-Ti alloys (at.%) at 900 °C for 960 h: (a) alloy 20# Ni₅₀Ti₃₀Cu₂₀; (b) alloy 26# Ni₄₅Ti₃₀Cu₂₅; (c) alloy 16# Ni₆₀Ti₂₅Cu₁₅; (d) alloy 15# Ni₅₅Ti₃₀Cu₁₅; (e) alloy 37# Ni₃₂Ti₂₀Cu₄₈; (f) alloy 35# Ni₄₈Ti₂₀Cu₃₂

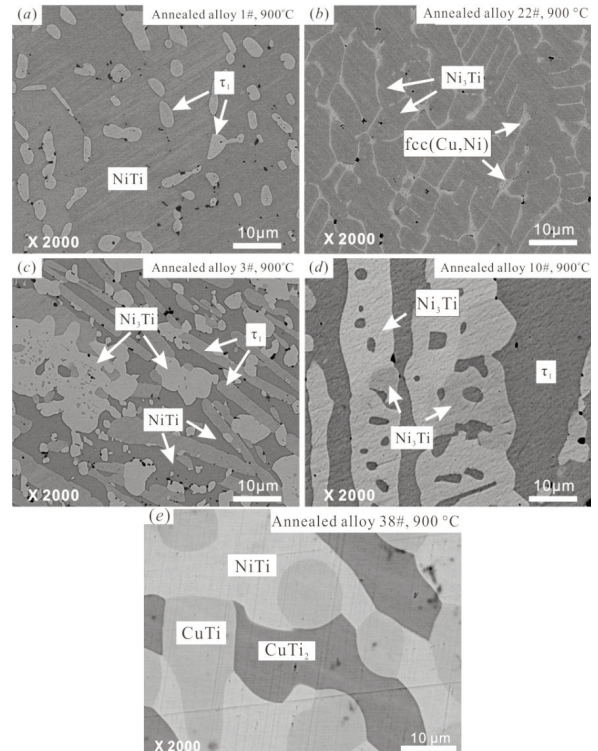


Figure 4. BSE images of the annealed Cu-Ni-Ti alloys (at.%) at 900 °C for 960 h: (a) alloy 1# Ni₅₀Ti₅Cu₅; (b) alloy 22# Ni₆₀Ti₃₀Cu₁₀; (c) alloy 3# Ni₆₀Ti₃₅Cu₅; (d) alloy 10# Ni₆₀Ti₃₀Cu₁₀; (e) alloy 38# Ni₉Ti₅₅Cu₃₆

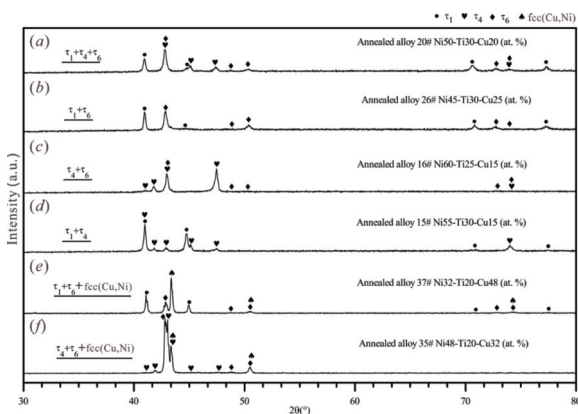


Figure 3. XRD patterns of the annealed Cu-Ni-Ti alloys (at.%) at 900 °C for 960 h: (a) alloy 20# Ni₅₀Ti₃₀Cu₂₀; (b) alloy 26# Ni₄₅Ti₃₀Cu₂₅; (c) alloy 16# Ni₆₀Ti₂₅Cu₁₅; (d) alloy 15# Ni₅₅Ti₃₀Cu₁₅; (e) alloy 37# Ni₃₂Ti₂₀Cu₄₈; (f) alloy 35# Ni₄₈Ti₂₀Cu₃₂

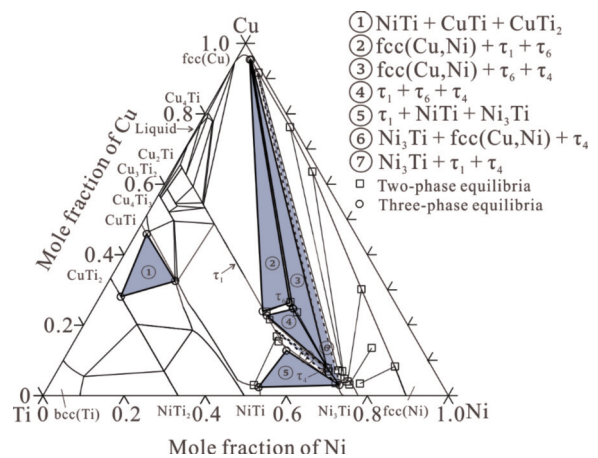


Figure 5. Isothermal section of the Cu-Ni-Ti system at 900 °C constructed with the experimental data of this work



determination by Loo et al. [20], the coordinates of the tie-triangles NiTi + CuTi + CuTi₂, fcc(Cu,Ni) + τ₁ + τ₆, fcc(Cu,Ni) + τ₄ + τ₆, τ₁ + τ₄ + τ₆ and τ₁ + NiTi + Ni₃Ti were experimentally determined in this work, as shown in Fig. 5.

3.2. Liquidus surface

In order to understand the solidification sequence and reaction type, microstructure of the as-cast alloys in the Ni-rich corner was analyzed using the results from SEM, EPMA and XRD. In accordance with the primary phase, the investigated alloys could be classified into six groups: the first group including the alloys 1#, 2# and 8# exhibits the primary phase of NiTi, the second group including the alloys 9#, 14#, 19#, 25# and 26# exhibits the primary phase of τ₁, the third group including the alloys 3#, 4#, 10#, 11# and 16# has τ₄ as the primary phase, the fourth group including the alloys 20#, 27#, 31#, 35# and 37# has τ₆ as the primary phase, the fifth group including the alloys 5#, 6#, 12#, 13#, 17#, 18#, 22#, 23#, 28#, 29#, 32#, 33# and 36# exhibits Ni₃Ti as the primary phase, and the sixth group including the alloys 7#, 24#, 30# and 34# has fcc(Cu,Ni) as the primary phase. According to the solidification paths, the as-cast alloys could be divided into 10 classes, and detailed analysis is given below. The identified phases and their compositions are presented in Table 3. The results for some representative alloys are discussed below.

Fig. 6 presents the microstructure and XRD pattern of the as-cast alloy 8#. As shown in Figs. 6(a) and 6(b), two phases could be seen distinctly: the dark primary NiTi phase and the grey phase τ₁. Besides, the eutectic NiTi + τ₁ structure could be seen in the

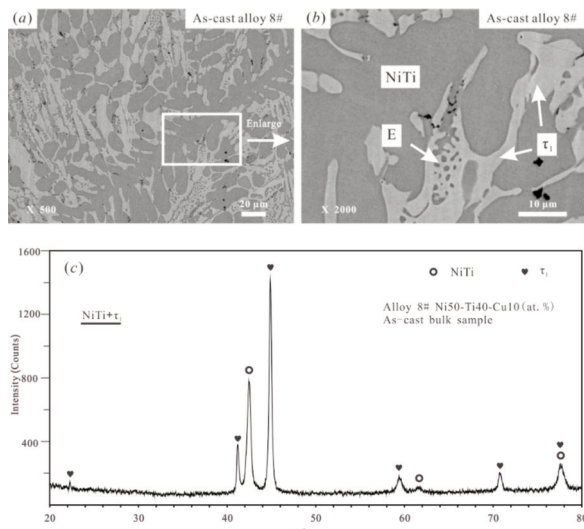


Figure 6. BSE images and XRD pattern of the as-cast alloy 8# Ni₃₀Ti₄₀Cu₁₀ (at.%) with the primary phase of NiTi: (a-b) BSE images; (c) XRD pattern

vicinity of the primary NiTi. Therefore, a eutectic reaction $L \rightarrow \text{NiTi} + \tau_1$ could be asserted. Based on the analysis, the sequence of the phase formation from the liquid phase with decreasing temperature could be specified as $L \rightarrow \text{NiTi}$, $L \rightarrow \text{NiTi} + \tau_1$.

Microstructures and XRD patterns of the as-cast alloys 14# and 26# are presented in Fig. 7. As shown in the BSE images of these two alloys, primary phase τ₁ could be easily observed. Furthermore, for the as-cast alloy 14#, the dark phase NiTi and many two-phase eutectic structures of τ₁ + NiTi could be determined in the micrograph (Figs. 7(a)-(b)), which means a reaction $L \rightarrow \text{NiTi} + \tau_1$ occurs during the solidification. Therefore, the solidification sequence of the phase formation from the liquid could be deduced in this alloy: $L \rightarrow \tau_1$, $L \rightarrow \text{NiTi} + \tau_1$. Figs. 7(c) and 7(d) display the micrograph of the as-cast alloy 26#. Different from the alloy 14#, the continuous phase τ₆ was formed adjacent to the primary phase τ₁. It indicates that a eutectic reaction $L \rightarrow \tau_1 + \tau_6$ exists. In addition, some fine three-phase structures τ₁ + τ₆ + fcc(Cu,Ni) could be observed, which suggests that the ternary eutectic reaction $L \rightarrow \tau_1 + \tau_6 + \text{fcc}(\text{Cu,Ni})$ takes place at the final stage of solidification. Hence, the solidification path in the alloy 26# could be deduced as $L \rightarrow \tau_1$, $L \rightarrow \tau_1 + \tau_6$, $L \rightarrow \tau_1 + \tau_6 + \text{fcc}(\text{Cu,Ni})$.

Figs. 8(a-f) present the BSE images of the as-cast alloys 3#, 10# as well as 16#, and Fig. 8(g) shows the

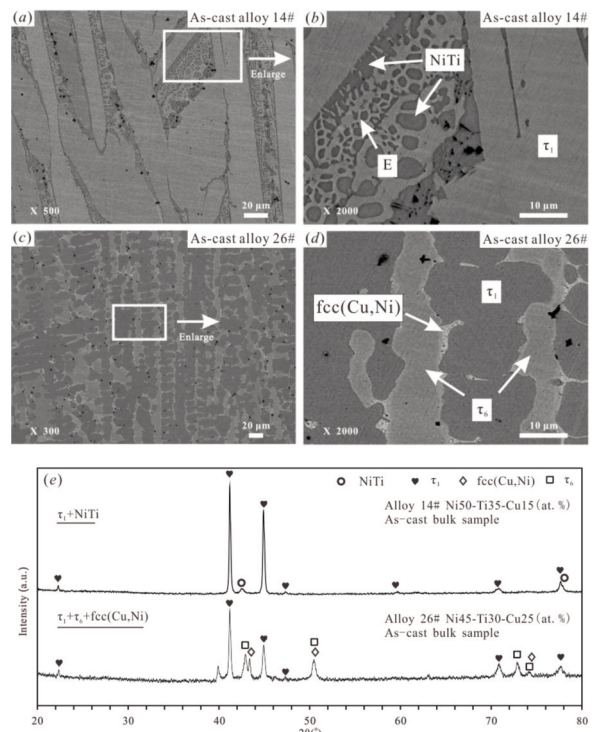


Figure 7. BSE images of the as-cast alloys (at.%) with the primary phase of τ₁: (a-b) alloy 14# Ni₅₀Ti₃₅Cu₁₅; (c-d) alloy 26# Ni₄₅Ti₃₀Cu₂₅. (e) XRD patterns of alloys 14# and 26#



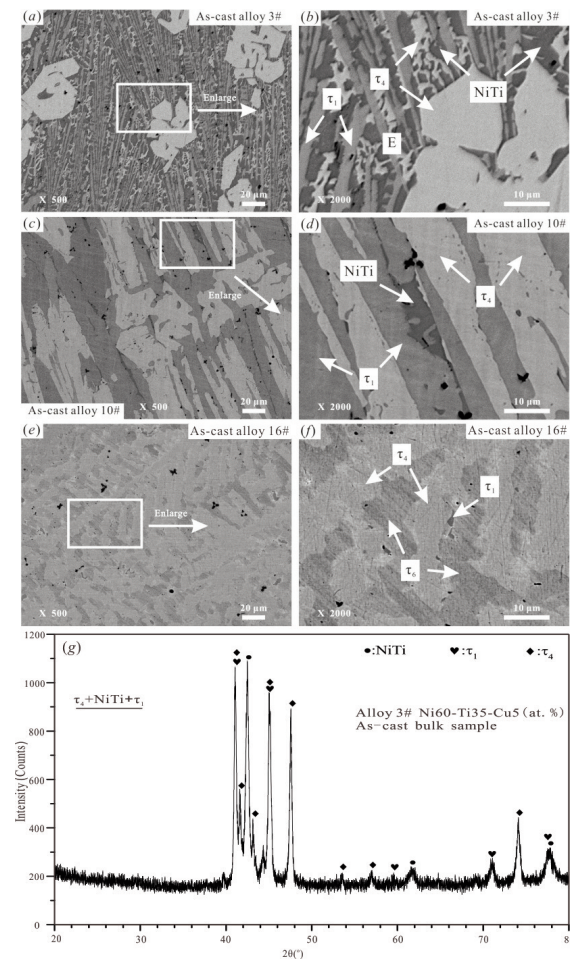


Figure 8. BSE images of the as-cast alloys with the primary phase of τ_4 (at.%): (a-b) alloy 3# $Ni_{60}Ti_{35}Cu_5$; (c-d) alloy 10# $Ni_{60}Ti_{30}Cu_{10}$; (e-f) alloy 16# $Ni_{60}Ti_{25}Cu_{15}$; (g) XRD pattern of alloy

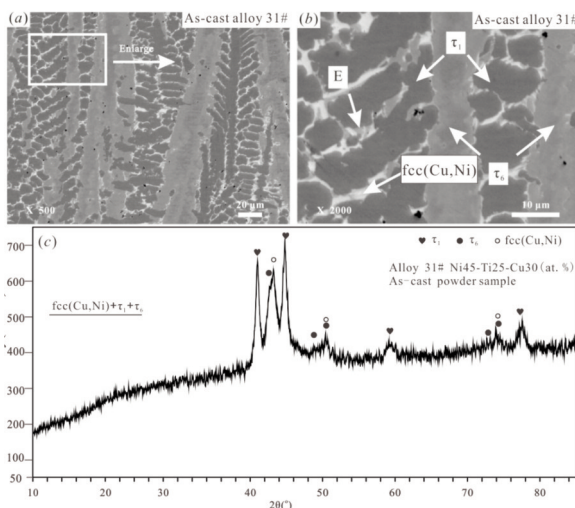


Figure 9. BSE images and XRD pattern of the as-cast alloy 31# $Ni_{45}Ti_{25}Cu_{30}$ (at.%) with the primary phase of τ_6 : (a-b) BSE images; (c) XRD pattern

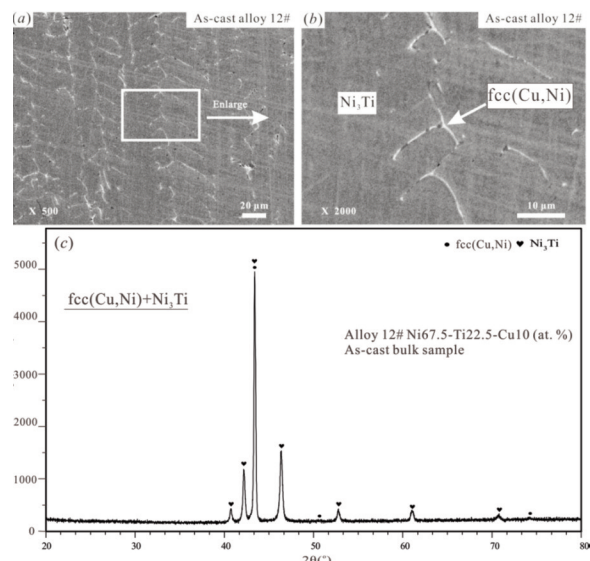


Figure 10. BSE images and XRD pattern of the as-cast alloy 12# $Ni_{67.5}Ti_{22.5}Cu_{10}$ (at.%) with the primary phase of Ni_3Ti : (a-b) BSE images; (c) XRD pattern

XRD patterns of the as-cast alloy 3#. From the BSE images of these alloys, it is evident that the primary phase is τ_4 in these alloys. In Figs. 8(a) and 8(b) for the alloy 3#, two-phase eutectic $\tau_4 + NiTi$ structure could be observed in the vicinity of the primary phase τ_4 , which means that a eutectic reaction $L \rightarrow \tau_4 + NiTi$ has taken place. Besides, the three-phase eutectic $\tau_4 + NiTi + \tau_1$ structure could be observed in some regions, which implies that the ternary eutectic reaction $L \rightarrow \tau_4 + NiTi + \tau_1$ has taken place at the final stage of solidification. Therefore, the solidification sequence of this alloy could be deduced as: $L \rightarrow \tau_4$, $L \rightarrow \tau_4 + NiTi$, $L \rightarrow \tau_4 + NiTi + \tau_1$. Compared with the microstructure of the as-cast alloy 3#, there is the grey τ_1 phase around the primary τ_4 phase for the alloy 10# in Figs. 8(c) and 8(d), indicating that the reaction $L \rightarrow \tau_4 + \tau_1$ could be asserted. In addition, the dark phase $NiTi$ could be seen, which coexists with the τ_4 and τ_1 phases suggesting the occurrence of a ternary eutectic reaction $L \rightarrow \tau_4 + \tau_1 + NiTi$. Hence, the solidification sequence of the alloy 10# could be deduced as: $L \rightarrow \tau_4$, $L \rightarrow \tau_4 + \tau_1$, $L \rightarrow \tau_4 + \tau_1 + NiTi$. Different from the alloys 3# and 10#, the τ_6 phase in the alloy 16# is encompassed by τ_4 phase, which suggests that the eutectic reaction $L \rightarrow \tau_4 + \tau_6$ takes place during the solidification, as shown in Figs. 8(e) and 8(f). In addition, the tiny phase τ_1 at the border between the τ_4 and τ_6 phases, could be observed. It means this three-phase eutectic structure $\tau_4 + \tau_6 + \tau_1$ formed in the final solidification. Therefore, the solidification sequence of this alloy could be deduced as: $L \rightarrow \tau_4$, $L \rightarrow \tau_4 + \tau_6$, $L \rightarrow \tau_4 + \tau_6 + \tau_1$.

Fig. 9 exhibits the microstructure and XRD pattern of as-cast alloy 31#. The matrix phase τ_6 could be

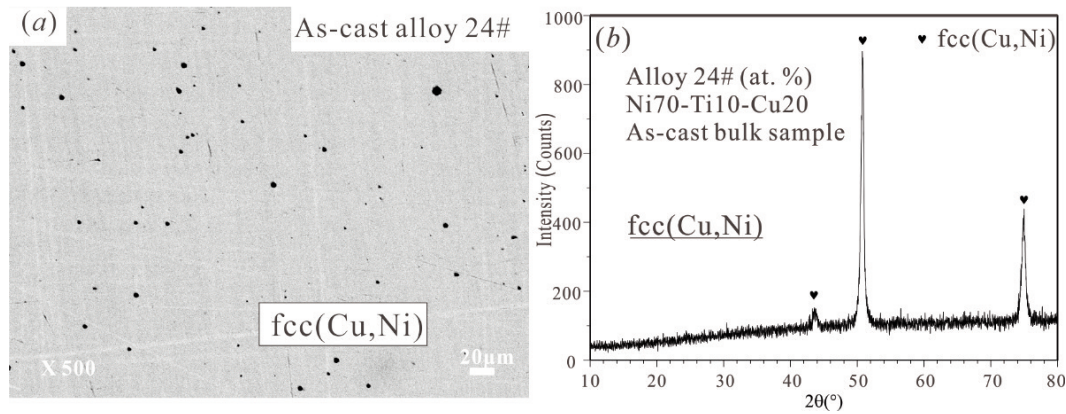


Figure 11. BSE image and XRD pattern of the as-cast alloy 24# Ni₇₀Ti₁₀Cu₂₀ (at.%) with the primary phase of fcc(Cu,Ni): (a) BSE image; (b) XRD pattern

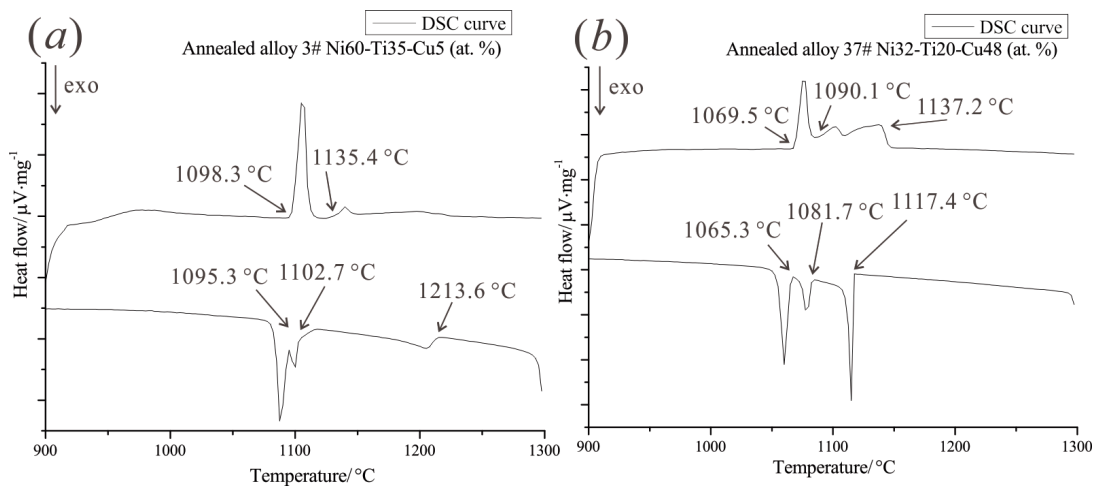


Figure 12. DSC results with heating and cooling curves of the annealed Cu-Ni-Ti alloys (at.%) at 900 °C for 960 h: (a) alloy 3# Ni₆₀Ti₃₅Cu₅; (b) alloy 37# Ni₃₂Ti₂₀Cu₄₈

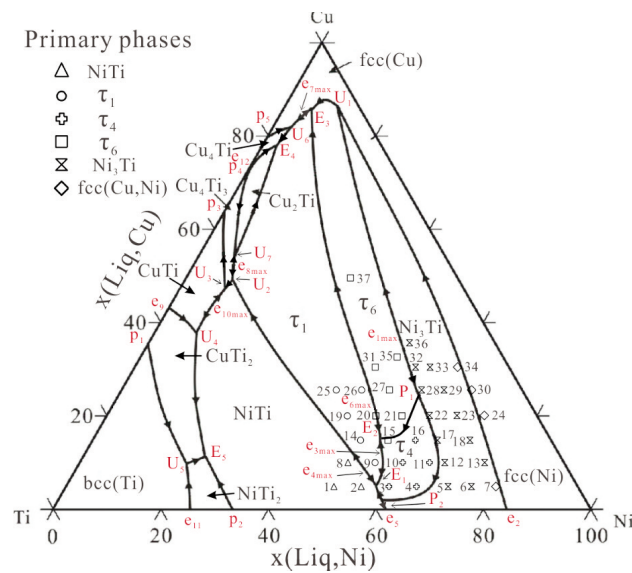


Figure 13. Experimental determined liquidus projection of the Cu-Ni-Ti system

evidently seen in Fig. 9(a). The enlarged part of the BSE image shows large amount of oval τ_1 phase near the primary phase τ_6 (Fig. 9(b)). The lamellar fcc(Cu,Ni) phase could be observed in the micrograph and the three-phase eutectic $\tau_6 + \tau_1 + \text{fcc}(\text{Cu,Ni})$ occurred during the final solidification. Therefore, the solidification sequence of alloy 31# could be $L \rightarrow \tau_6$, $L \rightarrow \tau_6 + \tau_1$, $L \rightarrow \tau_6 + \tau_1 + \text{fcc}(\text{Cu,Ni})$.

Microstructure and XRD pattern of the as-cast alloy 12# are shown in Fig. 10. Obviously, primary phase Ni_3Ti , white lamellar phase fcc(Cu,Ni) and two-phase eutectic structure $\text{Ni}_3\text{Ti} + \text{fcc}(\text{Cu,Ni})$ -morphology are presented in Fig. 10(a) and its enlarged image Fig. 10(b). It indicates that the Ni_3Ti phase precipitated firstly, then the two-phase eutectic structures formed during the solidification process. Therefore, the solidification sequence of this alloy from the liquid phase with decreasing temperature could be deduced: $L \rightarrow \text{Ni}_3\text{Ti}$, $L \rightarrow \text{Ni}_3\text{Ti} + \text{fcc}(\text{Cu,Ni})$.

From the microstructure and XRD pattern for the as-cast alloy 24#, as shown in Fig. 11, we can see that fcc(Cu,Ni) precipitated as primary phase and the liquid phase composition moving along the fcc(Cu,Ni) phase surface during the solidification process. Therefore, the solidification path of alloy 24# could be determined as $L \rightarrow \text{fcc}(\text{Cu,Ni})$.

DSC results of the selected annealed alloys are presented in Table 4 and Fig. 12. For the annealed alloy 3#, two peaks during heating and three peaks during cooling could be seen in Fig. 12(a). As shown in Fig. 4(c) and Figs. 8(a-b), the alloy annealed at 900 °C has a three-phase $\tau_1 + \text{Ni}_3\text{Ti} + \text{NiTi}$ microstructure for 960 h while τ_4 , NiTi as well as τ_1 phases are observed in the as-cast state. Comparing the BSE images in the same magnification for the alloys in annealed state and the as-cast state, we can see that the amount of NiTi is reduced while that of τ_1 is increased after annealing. According to the isothermal section at 900 °C (Fig. 5), the two-phase region of $\tau_1 + \text{Ni}_3\text{Ti}$ exists at this temperature suggesting that the solid-state invariant reaction $\text{NiTi} + \tau_4 \rightarrow \tau_1 + \text{Ni}_3\text{Ti}$ can be assigned to the first peak at 1098.3 °C on the heating curve. The peak at 1102 °C on the cooling represents the invariant ternary eutectic equilibrium $L \rightarrow \tau_4 + \text{NiTi} + \tau_1$, which is also observed for the annealed alloy 9#, as shown in Table 4. And the peak at 1135.4 °C on the heating represents the monovariant transition of eutectic type $L \rightarrow \tau_4 + \text{NiTi}$ at 1135.4 °C. The peak at 1213.6 °C on the cooling curve of the sample 3# corresponds to the primary phase formation reaction $L \rightarrow \tau_4$. However, no thermal effect was detected on the heating curve. The DSC curves of the annealed alloy 37# show three peaks during heating and cooling in Fig. 12(b). Three phases, τ_6 , τ_1 and fcc(Cu,Ni), were observed in both as-cast and annealed alloys, as shown in Table 3 and Fig. 2(e).

Therefore, according to the solidification sequence, three peaks were characterized as $L \rightarrow \tau_6 + \tau_1 + \text{fcc}(\text{Cu,Ni})$ at 1069.5 °C, $L \rightarrow \tau_6 + \tau_1$ at 1090.1 °C, $L \rightarrow \tau_6$ at 1137.2 °C, respectively, as listed in Table 4.

The liquidus projection was drawn to be consistent with the experimentally determined primary crystallization phases, solidification sequences and DSC results from this work. The ternary alloy compositions in this work are displayed and marked in Fig. 13. In the present work, we focused on the Ni-rich corner (more than 32 at.%), so the liquidus surface beyond this composition was from the literature [12, 17, 18]. The primary phase regions of τ_1 and NiTi meet with the $L + \tau_1 + \text{NiTi}$ monovariant line as shown in Fig. 13. And the primary phase regions of τ_1 and τ_6 merge with the $L + \tau_1 + \tau_6$ monovariant line. This implies that after the primary nucleation of the τ_1 phase, the solidification course could pass along the $L + \tau_1 + \text{NiTi}$ monovariant line (corresponding to $\tau_1 + \text{NiTi}$ eutectic microstructure) or the $L + \tau_1 + \tau_6$ monovariant line (corresponding to $\tau_1 + \tau_6$ microstructure). Microstructures of the alloys 14# and 26# in Fig. 7 and the DSC result of alloy 9# (Table 4) confirmed this conclusion. As shown in Fig. 13, the primary phase regions of τ_4 and NiTi merge with the $L + \tau_4 + \text{NiTi}$ monovariant line, while the primary phase regions of τ_4 and τ_1 or τ_4 and τ_6 meet with the $L + \tau_4 + \tau_1$ or $L + \tau_4 + \tau_6$ monovariant line respectively, which indicates that the solidification path could pass along the $L + \tau_4 + \text{NiTi}$ monovariant line or the $L + \tau_4 + \tau_1$ monovariant line, or the $L + \tau_4 + \tau_6$ monovariant line after the primary nucleation of the τ_4 phase. There will be three cases of microstructure with solidification paths: when passing along the $L + \tau_4 + \text{NiTi}$ line, the primary τ_4 could be surrounded by the eutectic $\tau_4 + \text{NiTi}$; when passing along the $L + \tau_4 + \tau_1$ line, it should be surrounded by τ_1 phase; when passing along the $L + \tau_4 + \tau_6$ line, it should be surrounded by the τ_6 phase, which is consistent with the observation of BSE images (Fig. 8) and the DSC result of alloy 3# in Fig 12(a). As shown in Fig. 13, the primary phase regions of τ_6 and τ_1 meet with the $L + \tau_6 + \tau_1$ monovariant line, which suggests that the solidification path could pass along this monovariant line after the primary nucleation of the τ_6 phase. Microstructure of alloy 31# (Fig. 9) and DSC result of alloy 37# (Fig. 12(b)) are consistent with this conclusion. The primary phase regions of Ni_3Ti and fcc(Cu,Ni) merge with the $L + \text{Ni}_3\text{Ti} + \text{fcc}(\text{Cu,Ni})$ monovariant line as shown in Fig. 13, which indicates that the solidification path could pass along the $L + \text{Ni}_3\text{Ti} + \text{fcc}(\text{Cu,Ni})$ monovariant line after the primary nucleation of the Ni_3Ti phase. Microstructure of the alloy 12# in Fig. 10 was in agreement with this conclusion. The corresponding reaction scheme of the liquidus projection is given in Fig. 14.



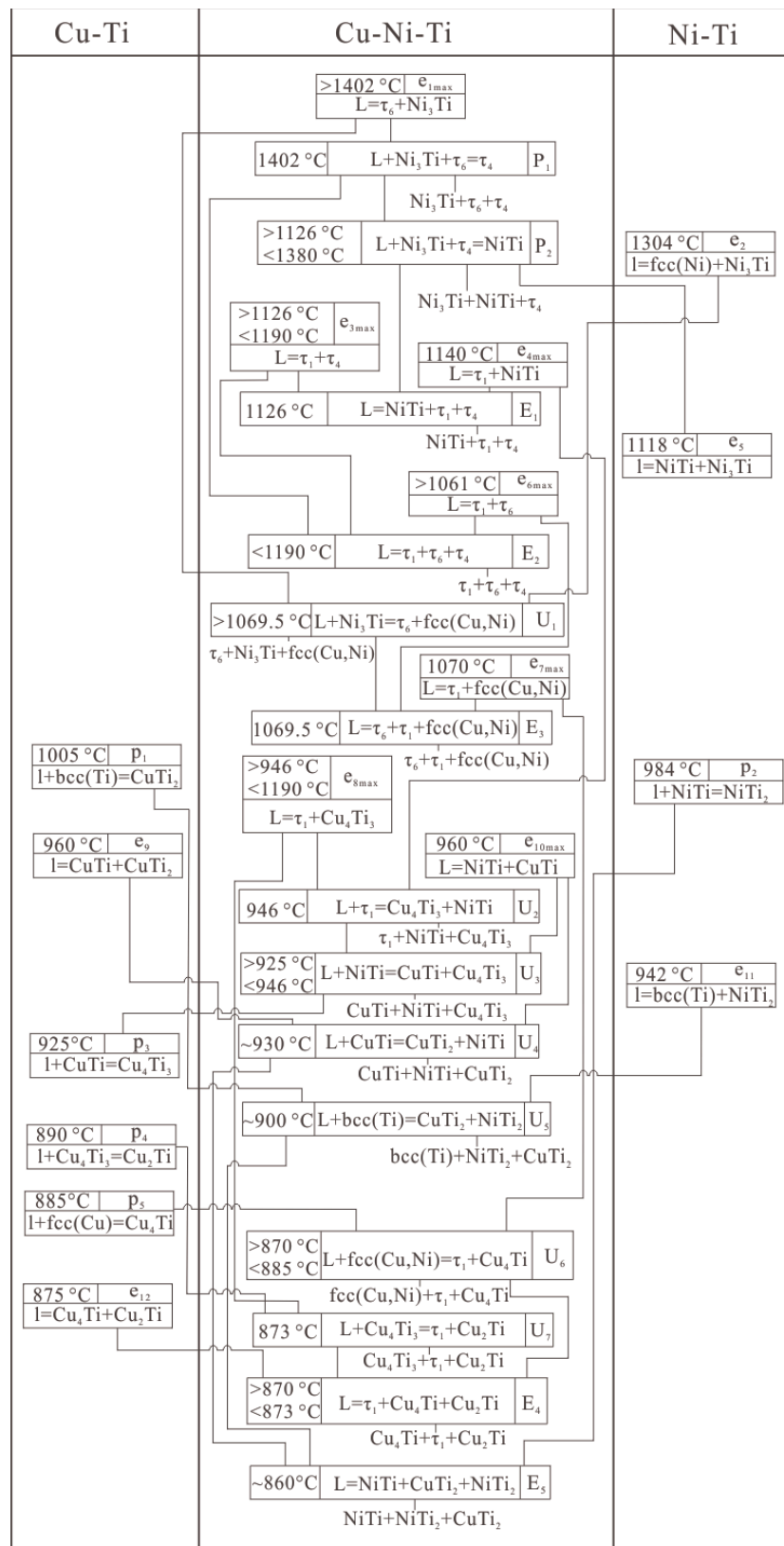


Figure 14. Reaction scheme for liquid in the Cu-Ni-Ti system with temperature in °C. The invariant reactions among solid phases are not included



4. Summary

Phase equilibria at 900 °C and liquidus projection in the Ni-rich corner of the Cu-Ni-Ti ternary system were experimentally investigated through XRD, SEM, EPMA and DSC measurements. Six two-phase and five three-phase regions at 900 °C were experimentally determined by annealed samples. Experimental results from the annealed samples indicate that the low-temperature ternary compound (τ_6) remains stable up to 900 °C, while the reported high-temperature compound (τ_5) was not observed at this temperature. By analyzing the phase composition and microstructure of the as-cast alloys, the primary phase τ_4 was experimentally determined, and the corresponding solidification paths were identified. Based on the experimental results of this work as well as the reliable literature information, the isothermal section at 900 °C and liquidus projection of Cu-Ni-Ti system as well as the reaction scheme are constructed, which shall be used in the following thermodynamic modeling of the Cu-Ni-Ti ternary system.

Acknowledgement

The financial support from the project of Innovation-driven Plan in Central South University (Grant No. 2015CX004), Ministry of Industry and Information Technology of China (Grant No. 2015ZX04005008) and the National Key Research and Development Program of China (Grant No. 2017YFB0701700) are acknowledged.

References

- [1] J.M. Jani, M. Leary, A. Subic, M.A. Gibson, *Mater. Des.*, 56 (2014) 1078-1113.
- [2] J.A. Shaw, S. Kyriakides, *J. Mech. Phys. Solids*, 43(8) (1995) 1243-1281.
- [3] S. Kozuh, L. Vrsalovic, M. Gojic, S. Gudic, B. Kosec, *J. Min. Metall., Sect. B*, 52 (2016) 53-61.
- [4] Y. Shugo, F. Hasegawa, T. Honma, *Bull. Res. Inst. Min. Dressing Metall. Tohoku Univ.*, 37(1) (1981) 79-88.
- [5] K. Melton, O. Mercier, *Metall. Trans. A*, 9 (1978) 1487-1488.
- [6] O. Mercier, K.N. Melton, *Metall. Trans. A*, 10(3) (1979) 387-389.
- [7] T.W. Duerig, K. Melton, D. Stöckel, *Engineering aspects of shape memory alloys*, Butterworth-Heinemann 1990.
- [8] V.A. Likhachev, S.R. Shimanskiy, *Fiz. Met. Metalloved.*, 58(4) (1984) 822-823.
- [9] B.S. Murty, M.M. Rao, S. Ranganathan, *Mater. Sci. Eng., A*, 196(1-2) (1995) 237-241.
- [10] P. Nash, *ASM International(USA)*, (1991) 394.
- [11] J.L. Murray, *ASM International, Materials Park, OH*, (1987) 197-211.
- [12] J.C. Schuster, G. Cacciamani, Germany: Springer-Verlag, (2005) 266-283.
- [13] H.U. Pfeifer, S. Bhan, K. Schubert, *J. Less Common Met.*, 14(3) (1968) 291-302.
- [14] V. Fedorov, M. Zakharov, V. Kucherov, O. Osintsev, *Russ. Metall.*, (6) (1971) 128-131.
- [15] F.J.J.V. Loo, G.F. Bastin, A.J.H. Leenen, *J. Less-Common Met.*, 57(1) (1978) 111-121.
- [16] M. Yakushiji, Y. Kondo, K. Kamei, *J. Jpn. Inst. Met.*, 44(6) (1980) 620-624.
- [17] H. Zhang, Y. He, F. Yang, H. Liu, Z. Jin, *Thermochim. Acta*, 574 (2013) 121-131.
- [18] W.J. Zhu, L.I. Duarte, C. Leinenbach, *Calphad*, 47 (2014) 9-22.
- [19] M. Yakushiji, Y. Kondo, K. Kamei, *J. Jpn. Inst. Met.*, 46(6) (1982) 571-577.
- [20] F.J.J.v. Loo, G.F. Bastin, *Diffusion in Metals and Alloys: International conference, Tihany, Hungaria*, (1982) 580-592.
- [21] K. Jozst, *Prace Inst. Hutniczych*, 19 (1967) 303-313.
- [22] F. Staub, K. Goszt, *Zeszyty Naukowe, Politech. Slaska*, 189(3) (1967) 31-36.
- [23] S.P. Alisova, N.V. Volynskaya, P.B. Budberg, A.N. Kobylkin, *Metally*, (1986) 210-212.
- [24] W. Tang, R. Sandstrom, S. Miyazaki, *J. Phase Equilib.*, 21(3) (2000) 227-234.
- [25] W. Tang, R. Sandstrom, Z.G. Wei, S. Miyazaki, *Metall. Mater. Trans. A*, 31(10) (2000) 2423-2430.
- [26] M. Lambrigger, *J. Phys. Chem. Solids*, 52(7) (1991) 913-914.
- [27] A. Taylor, R. Floyd, *J. Inst. Met.*, 80(11) (1952) 577-587.
- [28] N.N. Sirota, T.E. Zhabko, *Phys. Status Solidi A*, 63(2) (1981) K211-K215.
- [29] Y. Mishima, S. Ochiai, T. Suzuki, *Acta Metall.*, 33(6) (1985) 1161-1169.
- [30] V.F. Laves, H.J. Wallbaum, *Zeitschrift für Kristallographie-Crystalline Materials*, 101(1-6) (1939) 78-93.
- [31] R. Schmidt, M. Schlereth, H. Wipf, W. Assmus, M. Mullner, *Journal of Physics: Condensed Matter*, 1(14) (1989) 2473.
- [32] M. Mueller, H. Knott, *Transactions of American Institute of Metallurgical Engineers*, 227(ANL-FGF-396) (1963).
- [33] A. Sinha, *Trans. Metall. Soc. AIME*, 245(2) (1969) 237-240.
- [34] V.N. Eremenko, Y.I. Buyanov, N.M. Panchenko, *Powder Metall. Met. Ceram.*, 9(5) (1970) 410-414.
- [35] K. Schubert, *Zeitschrift für Metallkunde*, 56(3) (1965) 197.
- [36] V.N. Eremenko, Y.I. Buyanov, S.B. Prima, *Powder Metall. Met. Ceram.*, 5(6) (1966) 494-502.
- [37] M. Nishida, T. Ueda, Y. Toyama, A. Chiba, *Mater. Sci. Forum*, 56-58 (1990) 599-604.



- [38] J.H.N.V. Vucht, J. Less Common Met., 11(5) (1966) 308-322. 44(6) (1980) 615-619.
- [39] K.P. Gupta, J. Phase Equilib., 23(6) (2002) 541-547. [41] S.P. Alisova, P.B. Budberg, Y.K. Kovneristy, Metally, (1992) 223-226.
- [40] M. Yakushiji, Y. Kondo, K. Kamei, J. Jpn. Inst. Met.,

EKSPERIMENTALNO ODREĐIVANJE FAZNE RAVNOTEŽE PRI 900 °C I TEČNE POVRŠINE U Cu-Ni-Ti SISTEMU

B. Jin ^a, X. Lu ^b, S. Liu ^{**}, D. Huang ^c, Y. Du ^a

^a Centralno –južni univerzitet; Glavna državna laboratorija za metalurgiju praha, Čangša, Kina

^b Univerzitet u Konektikatu, Odsek za nauku o materijalima i inženjerstvo & Institut za nauku o materijalima, Stors, SAD

^c Univerzitet u Guangsiju; Glavna laboratorija za preradu obojenih metala i materijale, Naning, Kina

Apstrakt

Fazna ravnoteža na 900 °C i projekcija u tečnom stanju u niklom bogatom uglu Cu-Ni-Ti ternarnog sistema ispitivani su rendgenskom difrakcijom (XRD), skenirajućim elektronskim mikroskopom (SEM), elektronskom mikro-analizom (EPMA), i diferencijalnom skenirajućom kalorimetrijom (DSC) kaljenih i izlivenih legura. Za izotermalni deo na 900 °C, nije pri visokim temperaturama primećeno ternarno jedinjenje (τ_3) koje se javlja u literaturi, ali je identifikovano da je odgovarajuće jedinjenje koje se javlja na niskim temperaturama (τ_6) na ovoj temperaturi stabilno. Za projekciju u tečnom stanju primarna faza τ_4 je eksperimentalno određena po prvi put, i povezani putevi solidifikacije identifikovani su pomoću eksperimentalnih podataka na izlivenim legurama. Detektovana je jedna invarijantna reakcija u čvrstom stanju, $NiTi + \tau_4 \rightarrow \tau_1 + Ni_3Ti$ na 1098.3 °C, i dve ternarne eutektičke reakcije, $L \rightarrow \tau_1 + \tau_4 + NiTi$ na 1126 °C and $L \rightarrow \tau_1 + \tau_6 + fcc(Cu,Ni)$ na 1069.5 °C. Shodno tome, data je i Scheil šema reakcije. Svi dobijeni eksperimentalni rezultati obezbeđiće pouzdane informacije za dalju termodinamičku optimizaciju ternarnog Cu-Ni-Ti sistema.

Ključne reči: Cu-Ni-Ti; Izotermalni deo; Termalna analiza; Projekcija u tečnom stanju; Šema reakcije

